JOURNAL OF SPACECRAFT AND ROCKETS
Vol. 45, No. 1, January–February 2008

Effective Modulus of Creased Thin Membranes

Kyeongsik Woo*
Chungbuk National University, Cheongju, Chungbuk 361-763, Republic of Korea
and
Kuldeep Nandukar† and Christopher H. Jenkins‡
Montana State University, Bozeman, Montana 59717

DOI: 10.2514/1.29282

In this study, the effective modulus of creased thin membranes was calculated by finite element analyses. Geometrically and materially nonlinear contact analyses were performed to simulate the entire process of creasing and uniaxial tensile testing. First, the creased geometry of thin membranes was predicted from a creasing simulation. The creased membranes were then subjected to a series of numerical uniaxial tensile tests to calculate the effective modulus. The creased and tensile geometries were also obtained by experiments and theoretical computations, respectively, and the results were compared. Numerical specimens with various crease gauges were considered to study the effect of the amount of creasing. The size effect of the specimen was also investigated.

Nomenclature

D	=	flexural stiffness
E	=	pristine membrane modulus
$E^*(\sigma)$	=	effective modulus of creased membrane under tensile load σ
$E^{*\prime}(\sigma)$	=	effective modulus of creased membrane by a series spring model
e	=	nominal strain
L_0	=	original uncreased membrane length
$\tilde{L}_0$	=	original length of elastic portion of creased membrane
$L^*(\sigma)$	=	nominal creased membrane length under tensile load σ
$L^{*\prime}(\sigma)$	=	nominal creased membrane length for a series spring model
P	=	applied tensile load
t	=	membrane thickness
x	=	coordinate value in the membrane length direction
y_0	=	distance to horizontal asymptote
Δl	=	numerical strain gauge length
δ	=	crease gauge
$\varepsilon_{\text{Mises}}$	=	Mises strain
θ	=	membrane angle
θ_0	=	crease angle
σ	=	applied nominal stress
σ_{Mises}	=	Mises stress

I. Introduction

THIN membranes are being extensively considered for use in large, ultralight gossamer space structures. Membrane structures can be made extremely light in mass, and packaged very small in volume. This advantage provides an ideal option for the Earth-made–space-deployed applications [1]. However, due to the almost nonexisting bending stiffness, thin membranes buckle almost immediately when compressed, which is called wrinkling. The wrinkling behavior is known to be dependent on the geometric and loading characteristics, as well as the material properties. One of the factors gaining importance is creasing. In the membrane structures for deployment in space, for example, solar sails, creases develop in a systematic and regular pattern from packaging (e.g., [2–4]). Creases resulting from membrane handling are inherently random [5].

The membrane wrinkle problems with creases have been analyzed using either membrane or shell approaches. Papa and Pellegrino [4] performed shell element postbuckling analysis to study the mechanics of systematically creased square membranes. While providing detailed solutions including the deformed creased topology, the shell analysis required a large number of elements to accurately model the fine deformation details. Gough et al. [6] used membrane elements for the analysis of a corner-loaded square membrane with transverse crease lines. In this study, a penalty-parameter material modeling was employed to account for the wrinkling, and the induced anisotropy due to creases was considered.

To use the membrane approach for creased membranes, one of the key issues is to correctly model the equivalent material property of the creased portion of the membrane, which is highly nonlinear and size dependent (see Fig. 1). Because of extreme compliance, the experimental characterization of the thin membranes is difficult. MacNeal and Robbins [7] developed an analytical model for transversely creased tape under a tensile load. They used elastic-plastic hinge beam theory to predict the crease topology from which the effective modulus was calculated. Murphy et al. [8] extended this model for coated membranes. In these studies, the creased hinge was simply assumed to behave elastically first and then become a perfectly plastic hinge after a certain load level. The derivation was limited to tightly creased cases in which the initial crease angle was assumed to be 90 deg. Also, the residual stress during creasing was not considered. Gough et al. [6] performed a series of experiments to measure the nonlinear properties. However, it was done for a relatively high stress range. Because of the severe measurement difficulty, the stress–strain curve in the low 7 kPa (1 psi) stress range that a solar sail membrane might be subjected to was not obtained. Hossain et al. [9] considered the nonlinear material response of systematically creased polymer membranes. They performed a series of experiments, also in a relatively high stress range, and the stress–strain relationship was observed for single and doubly creased Kapton. A strategy for the numerical simulation of single creased Kapton was presented and numerical results were validated with experimental values.

In this paper, the tensile behavior of creased thin membranes was studied by finite element (FE) analyses. First, a creasing process was simulated numerically to predict the creased membrane geometry

Presented as Paper 1798 at the 47th AIAA/ASME/ASCE/AHS/ASC Structures, Structural Dynamics, and Materials Conference, Newport, RI, 1–4 May 2006; received 14 December 2006; revision received 7 May 2007; accepted for publication 8 May 2007.

*Professor, Department of Structural Systems & CAE. Member AIAA.
†Research Assistant, Department of Mechanical and Industrial Engineering.
‡Professor and Head, Department of Mechanical and Industrial Engineering. Associate Fellow AIAA.

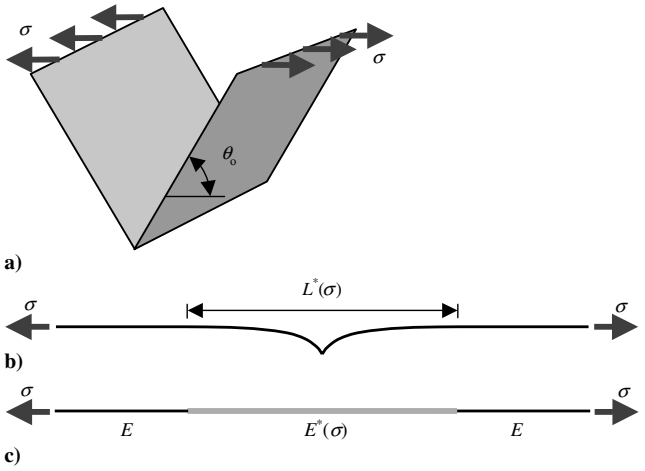

Fig. 1 An effective property modeling of the creased portion of the membrane under tension: a) undeformed, b) deformed, and c) effective.

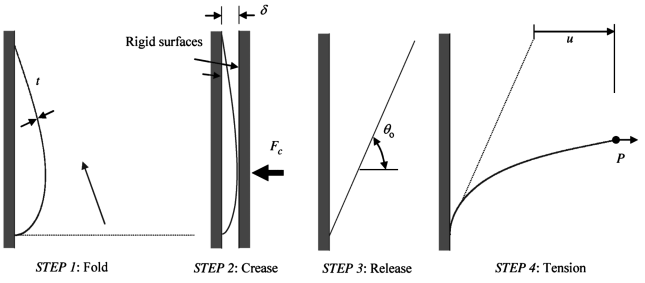

Fig. 2 Schematic of simulation steps for creasing and uniaxial tensile test.

including the crease angles. This was done using contact analysis. The creased membranes were then subjected to numerical uniaxial tensile tests to calculate the effective modulus. The creased and tensile geometries were also obtained by experiments and theoretical computations, respectively, and compared. Various crease gauges and specimen size were considered to study the effect on the variation of the effective modulus.

The specific contribution of this work to the field is the use of numerical experiments to determine the effective crease modulus of thin polymer films. Simulation is required due to the extreme measurement challenges involved with physical experiments that make the determination of this key material property cost prohibitive.

II. Analysis

To calculate the effective modulus of creased thin membranes, geometrically and materially nonlinear finite element analyses (FEA) were performed simulating the entire process of creasing and uniaxial tensile testing. The FE software ABAQUS was used for the computation.

Figure 2 shows the analysis steps schematically. The crease-release simulation is done in steps 1–3. Because of symmetry, one-half of the membrane in the length direction is modeled. The membrane mesh is folded first and then compressed to prescribed crease gauge (δ) by activating two rigid contact surfaces and pressing the right surface. Next, the membrane is released by removing the contact surfaces to give the crease topology after spring back, including the crease angle (θ_0). Finally, a tensile load (P) is applied at the tip of the membrane and the stress–strain curve is obtained, from which the effective modulus (E^*) is calculated.

In the analyses, the creasing gauge was varied representing a wide range of softer (larger δ) and harder (smaller δ) creases. It should be noted here that, for small crease gauge, computational instability occurs during creasing simulation. The upper portion of the membrane shown in step 2 in Fig. 2 is under almost no stress but very

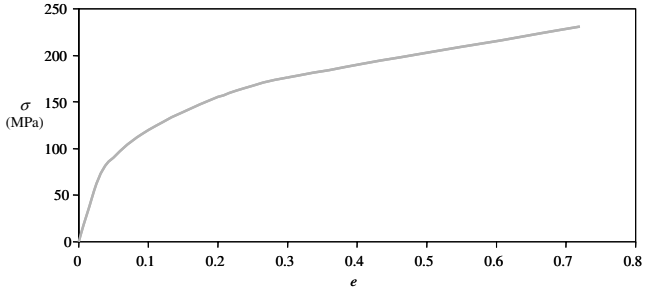

Fig. 3 Tensile stress (σ) strain (e) curve for Kapton-type HN, 25 μm (www.dupont.com/kapton).

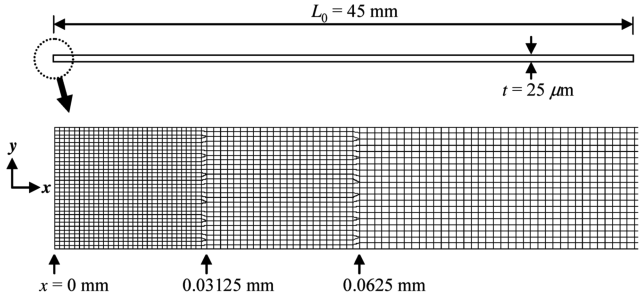

Fig. 4 Finite element mesh modeling.

susceptible to loading changes due to very small bending stiffness. As a result, when the membrane is highly creased, there occurs a snapping deformation at the lightly stressed upper part from a simple convex to a doubly curved configuration. To stabilize the computation, the *STATIC, STABILIZE option was used; the damping coefficient was kept just small enough for the computation to continue.

In this study, 25 μm (1 mil) thick Kapton-type HN film was simulated. The elastic modulus is 2.5 GPa and the Poisson's ratio is 0.34. The yielding occurs at 69 MPa, and the ultimate strength is 231 MPa. Figure 3 shows the stress–strain curve of the Kapton film. This curve was tabularized piecewise linearly for use in the plastic analysis. Mises yield surfaces were assumed with isotropic hardening. Perfectly plastic deformation was assumed to occur beyond the ultimate stress value.

Figure 4 shows the one-half portion of a 90-mm long membrane specimen. Because of symmetry, the half-portion was modeled in the analysis. The cross section of the membrane was modeled with 2-dimensional plane strain elements. The plane strain assumption was thought to be acceptable because the membrane is under a bending stress state predominantly during the creasing and mostly during the tensile loading until the applied load level becomes very high. The circled portion corresponds to the center region around the fold line where the crease occurs and thus was modeled with the highest mesh density as shown in the figure. The number of elements were gradually reduced as one moved away from the center region. Table 1 summarizes the number of thru-thickness elements and element types used. The total number of elements used was 9644. Elements with full integration were used for the highly refined portion near the fold line, whereas elements with reduced integration were used for regions where the number of thru-thickness elements was less than or equal to 10. This mesh was selected after a series of mesh convergence tests.

III. Experiment

The present experimental work followed from earlier work by Gough et al. [6]. In the present case, specimens used for the experiment were cut out from 1-mil thick Kapton membrane. As shown in Fig. 5, a rectangle of the size 90 × 10 mm^2 was marked on the sheet of Kapton by use of a template and specimens were cut out

Table 1 Number of thru-thickness elements and element types in finite element modeling

Range in the x direction, mm	No. of thru-thickness elements	Element types
0–0.03125	32	CPE4/CPE3
0.03125–0.0625	26	CPE4/CPE3
0.0625–0.0125	20	CPE4/CPE3
0.0125–0.25	16	CPE4/CPE3
0.25–0.5	12	CPE4/CPE3
0.5–1	10	CPE4R/CPE3
1–2	8	CPE4R/CPE3
2–4	6	CPE4R/CPE3
4–45	4	CPE4R/CPE3

by using a razor cutter. Care was taken to get regular geometry for each specimen.

The equipment for creasing mainly consisted of two metallic parallel walls, one fixed while the other can move relative to the fixed one. The movable wall can be precisely translated with the help of a vernier caliper. The final distance between the walls is notated as δ.

Specimens were lightly folded and placed between the two walls at a plate separation greater than δ. Then the plate separation was slowly decreased to δ and this value recorded. Because of viscoelastic effects, specimens were kept in the creased position for 10 h and then removed. Crease angle (θ_0) measurements were taken after a span of another 10 h to again account for viscoelastic effects. Angle measurements were taken using a protractor. The uncertainty estimate for the experiments was based on typical measurement uncertainty for the caliper and protractor used: crease gauge was 0.025 mm (0.001 in.) and crease angle was 0.5 deg.

For each value of δ, five specimens were tested and an average value of θ_0 was calculated. Results are provided in the following section.

IV. Results and Discussion

A. Crease Analysis

Figure 6 shows the history of the maximum Mises stress (σ_{Mises}) versus the crease gauge (δ). During creasing, the maximum stress occurred at the upper and lower sides of the symmetric fold line as indicated by the dotted circles in the figure. For hard creasing, the compressive upper side produced slightly larger stress than the tensile lower side. The yielding started to occur when $\delta = 0.530$ mm at the upper side and $\delta = 0.522$ mm at the lower side. At this load level, the yielding occurred only for a limited region around the upper and lower sides of the symmetry line, and did not produced any meaningful amount of permanent deformation. As the crease gauge reduced, the maximum stress increased gradually along with the amount of the yielded region. It can be noticed that perfectly plastic deformation occurred after the maximum Mises stress reached the material ultimate value at $\delta = 0.048$ mm and $\delta = 0.039$ mm at the upper and the lower sides, respectively.

Figure 7 shows the distribution of Mises stress for cases with various crease gauges. As can be seen in the figure, very high stresses occurred at the upper and the lower sides and almost all material yielded in the thickness direction when the crease gauges were small. The yielded or creased region was concentrated near the fold line. The magnitude of the Mises stress values quickly decreased when moved away from the crease line. The residual Mises stress distributions were plotted in Fig. 8. These are the stress distributions when the crease loads were removed and due to the permanent crease deformation. It can be seen that very high stresses still remained and were concentrated at the top and bottom surfaces near the fold plane. However, the signs of stress reversed due to the interaction of the surrounding region. That is, though the signs of the individual stress components were not seen in this figure, the originally highly compressed upper corner came under high tensile stress, while the lower corner was under compression. As with the creased state, the residual stresses with significant magnitude were distributed mainly near the fold line.

The history of σ_{Mises} at the upper and lower corners was plotted in Fig. 9. Here, $\varepsilon_{\text{Mises}}$ was defined as

$$\varepsilon_{\text{Mises}} = \sqrt{\frac{1}{2}[(\varepsilon_{xx} - \varepsilon_{yy})^2 + \varepsilon_{xx}^2 + \varepsilon_{yy}^2 + 6\varepsilon_{xy}^2]} \tag{1}$$

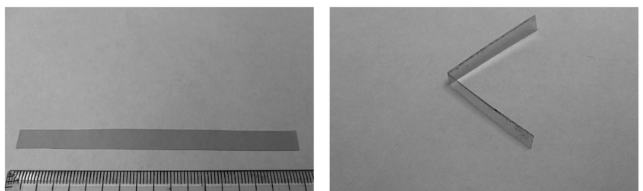

a) b)

Fig. 5 Kapton specimens: a) uncreased, and b) creased.

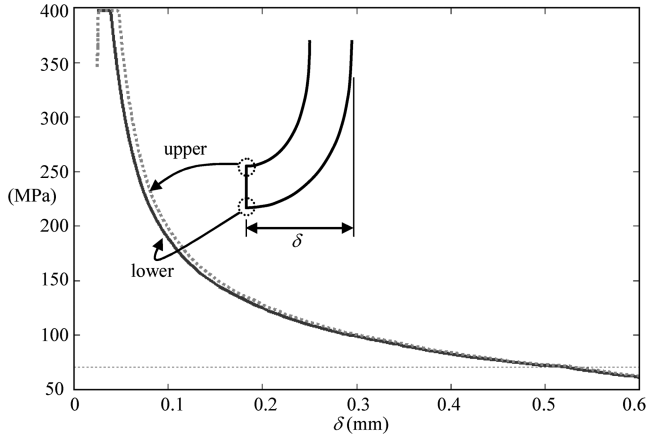

Fig. 6 History of the maximum Mises stress (σ_{Mises}) versus crease gauge (δ). The horizontal dotted line indicates the yield stress of 69 MPa.

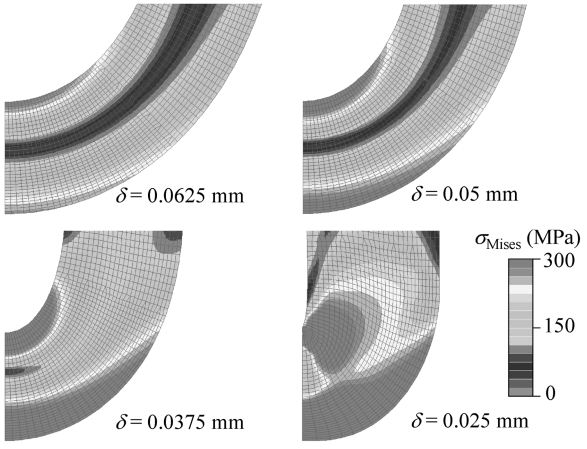

Fig. 7 Distribution of Mises stress at the creased state.

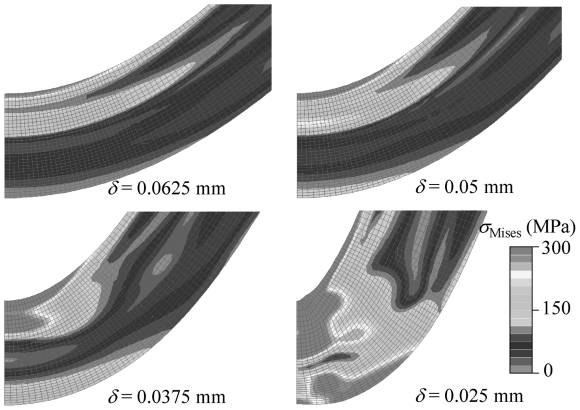

Fig. 8 Distribution of Mises stress at the release state.

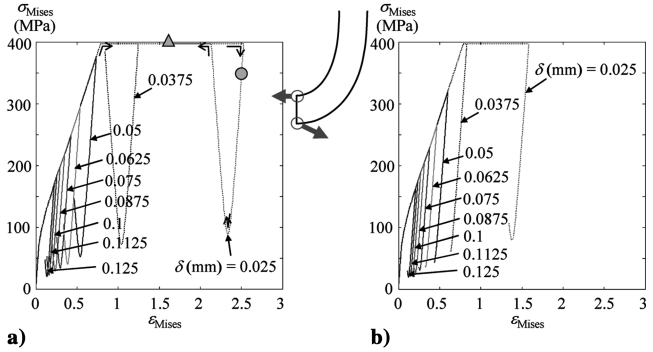

Fig. 9 Variation of σ_{Mises} and $\varepsilon_{\text{Mises}}$ for various crease gauges during crease and release processes at a) upper and b) lower corners. The circular and triangular marks are discussed in the text.

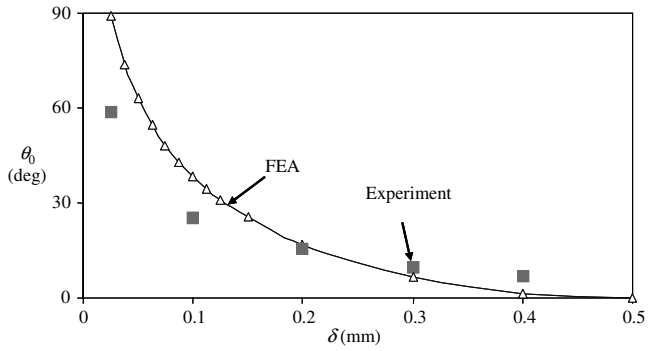

Fig. 10 Variation of crease angle versus crease gauge.

Though not possessing much physical meaning, this strain measure was used to give an idea of how the stress varied during the creasing and unloading processes. As can be seen in Fig. 9a, the σ_{Mises} at the upper corner increased against $\varepsilon_{\text{Mises}}$ during creasing. The σ_{Mises} reached the ultimate strength when the membrane was creased up to the crease gauge value $\delta = 0.048$ mm, after which perfectly plastic deformation occurred as assumed. When it was creased even further, there occurred so much plastic deformation that unloading initiated at the upper corner while the maximum stress started to occur away from the corner point. The circular mark in Fig. 9a indicates the σ_{Mises} value at the upper corner when the membrane was creased up to $\delta = 0.025$ mm. When the crease load was removed, the σ_{Mises} first decreased and then increased. During unloading, the σ_{Mises} value at the upper corner when $\delta = 0.025$ mm reached the ultimate values again and then stopped at the point indicated by a triangular mark. Similar patterns in the σ_{Mises} history were observed for other cases with larger crease gauges, having the turning points in the stress–strain curves during the release process. At the turning points, the stress states of the upper corner changed from compressive to tensile which can be understood from the discussion of Fig. 8. In the case of the lower corner, the σ_{Mises} values showed similar variation as shown in Fig. 9b. The curves also showed the tensile to compressive turning points during the release process. However, the σ_{Mises} values showed smaller variation compared to those of the upper corner and much less stress increases occurred after the turning points during the unloading.

Figure 10 shows the variation of the crease angle (θ_0) versus the crease gauge (δ). As seen in Fig. 1, the crease angle was defined as the angle between the horizontal axis and the midplane of the unstressed membrane. The crease angles by the analysis were numerically measured after removing the crease loads. As can be seen in Fig. 10, the analysis and the experimental results showed similar trends in variation. When the membrane was hard creased with smaller crease gauge distance, the analysis predicted higher crease angles. For a moderate crease range, however, both results agreed relatively well.

B. Tensile Behavior

Numerical tensile tests were performed for the finite element specimens of the creased Kapton membrane. Uniaxial tensile loads were applied to the tip of the numerical specimens containing the residual stresses from creasing, while the symmetry condition along the fold line was maintained (see step 4 in Fig. 2).

Figure 11 shows deformed meshes under tensile loads. These were the cases that were creased originally with $\delta = 0.025$ mm and 0.05 mm, respectively, then released and tensile loaded. The crease angles (θ_0) at the released state were 89.6 deg for $\delta = 0.025$ mm, and 62 deg for $\delta = 0.05$ mm. As can be seen in the figure, the creased thin membrane deformed significantly even under a very small tensile load due to the negligible bending stiffness. If one uses the zero-load released state as the baseline configuration, very large strain values are encountered. In this study, strains were calculated using the "1 psi" configuration (deformed geometry under 6.9 kPa or 1 psi load) as the baseline configuration unless otherwise noted.

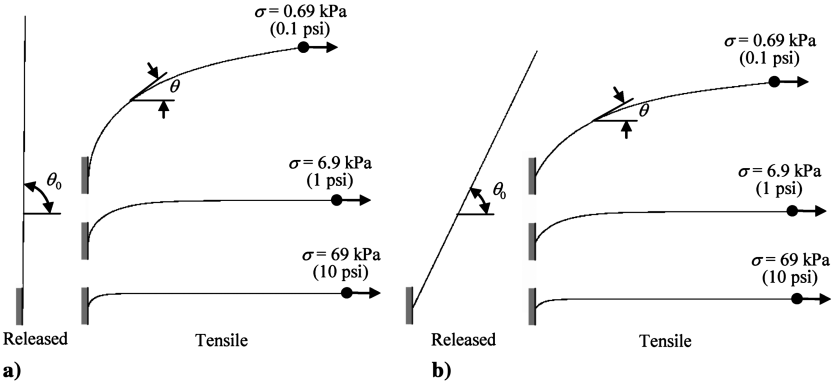

Fig. 11 Deformed meshes of creased membranes under tensile load: a) $\delta = 0.025$ mm, and b) $\delta = 0.05$ mm.

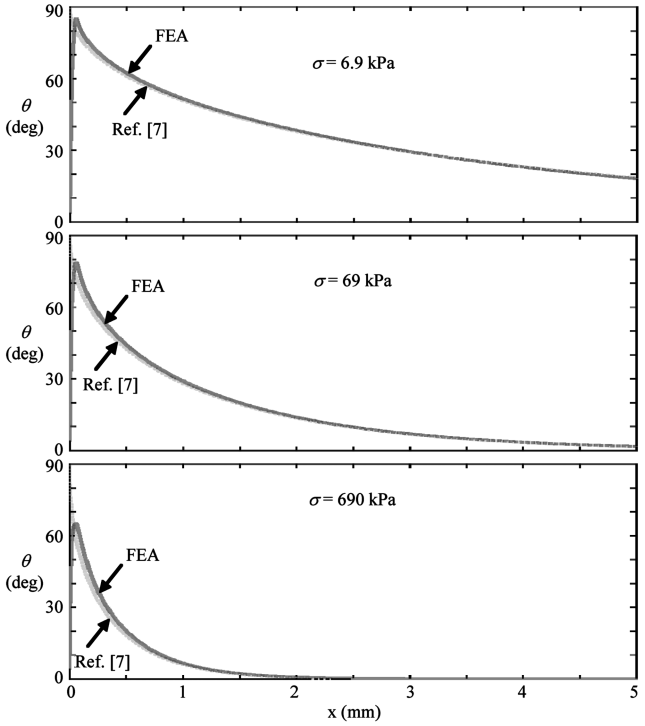

Fig. 12 Comparison of membrane angles under various tensile loads ($\delta = 0.025$ mm).

The membrane geometry under tensile load can be calculated by the following equation proposed by MacNeal and Robbins [7]:

$$\theta = \frac{\pi}{2} - \sin^{-1}\left(1 - \frac{P}{2D}(y - y_0)^2\right) \qquad y_0 = \sqrt{\frac{2D}{P}(1 - \cos\theta_0)} \quad (2)$$

where y_0 denotes the vertical distance from the creased tip to the horizontal asymptote, and P and D indicate the applied tensile load and flexural stiffness, respectively. The membrane angles calculated by Eq. (2) were compared to those by the finite element analysis in Fig. 12. This was for the case where the membrane was initially creased with the smallest crease gauge of $\delta = 0.025$ mm and thus with the largest crease angle. Here, the crease angle θ_0 calculated by the crease simulation was used in Eq. (2). In the figure, the angles were plotted for the range $0 < x < 5$ mm under three different load levels. As can be seen in the figure, the results agreed very well for all considered load levels, although differences occurred near the creased tip. This was due to the fact that the theory was not able to follow the local creased geometry near the fold line. As the tensile load increased, the differences tended to increase, but were not significant.

Figure 13 shows the variation of membrane angles versus the applied tensile load at various locations for the creased membrane with the crease gauge of $\delta = 0.025$ mm. As the load increased, the membrane angles decreased quickly from the initially large crease angle. At 6.9 kPa load (=1 psi), the angles in the range of $x <$ 20 mm was less than 2 deg and the membrane in this range can be considered to have reached its horizontal asymptote. The membrane angle measured at $x = 40$ mm was less than 2 deg at approximately 1.5 kPa. Thus, for the tensile load higher than this, the results calculated with the 45-mm length specimen can be considered acceptable. For other cases with larger crease gauges, smaller membrane angles occurred.

Figure 14 shows the stress–strain curves for the creased Kapton films. These are the results of the numerical uniaxial tensile tests. The actual tests were not performed due to the measurement difficulty because the applied forces would have to be very small. (For example, to produce 6.9 kPa stress acting on a 25 μm $\times$ 10 mm cross section, the applied force should be as small as 0.0017 N.) The strains were calculated by dividing the u displacements of the end

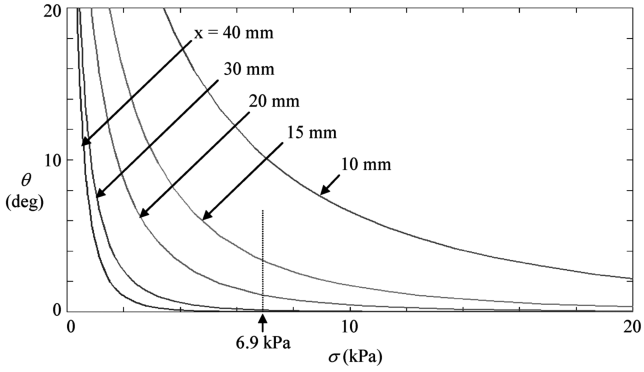

Fig. 13 Variation of membrane angles versus tensile load at various locations ($\delta = 0.025$ mm).

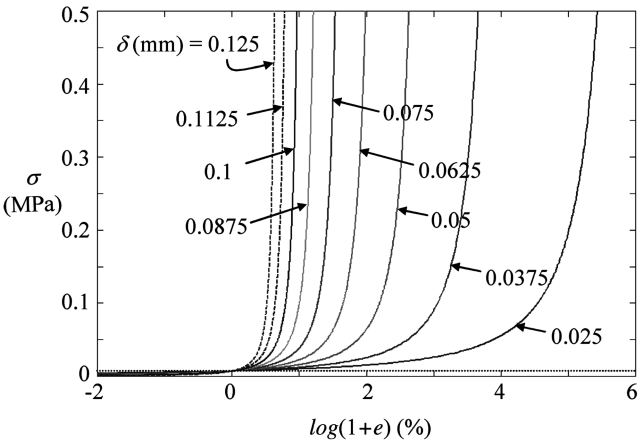

Fig. 14 Tensile stress–strain curves for membranes creased with various crease gauges. Strains were calculated from the "1 psi" configuration.

point by the x-coordinate values of the 1 psi baseline configuration, and then taking the log of the ratio. The stresses were defined as the applied load divided by the cross-sectional area. The figure shows that the stresses were initially very small, and kept small for a large portion of strain ranges. This was expected because very small forces were needed to bend the creased thin membranes. The strain range under small stress was much larger for the more hard creased cases with smaller crease gauges. As the creases were stretched out, however, the problem changed from bending to extensional and the forces started to increase rapidly. This can be clearly observed in the figure where the curves change rapidly from horizontal to vertical.

For better understanding of the tensile behavior, the stress–strain curves were plotted for a different strain measure in Fig. 15. In this case, the strains were calculated by dividing the end displacements by the uncreased original length. The figure was plotted by zooming in on the strain range where high stress variation occurred. As can be seen, the initially small stresses started to increase rapidly as the creased membranes were stretched to the original length. For the case with the smallest crease gauge of $\delta = 0.025$ mm, the stress was larger and started to increase faster. This is easily understandable considering that, having the hardest crease, this case had the largest disturbed region with permanent plastic deformation at the creased hinge and the largest crease angle, which required the faster increased force. For the case with smaller crease gauges, the stress increases were delayed because the amount of disturbance became less with decreased crease angles. Also seen in the figure is that the stress–strain relations became almost linear when the creased membranes were stretched out more than the original length. The stress–strain curves in this strain range were plotted in Fig. 15b which is the zoom-in view of the circled region in Fig. 15a. As can be seen in this figure, the curves are almost linear indicating that the deformations are fully extensional. Note that the cases with larger

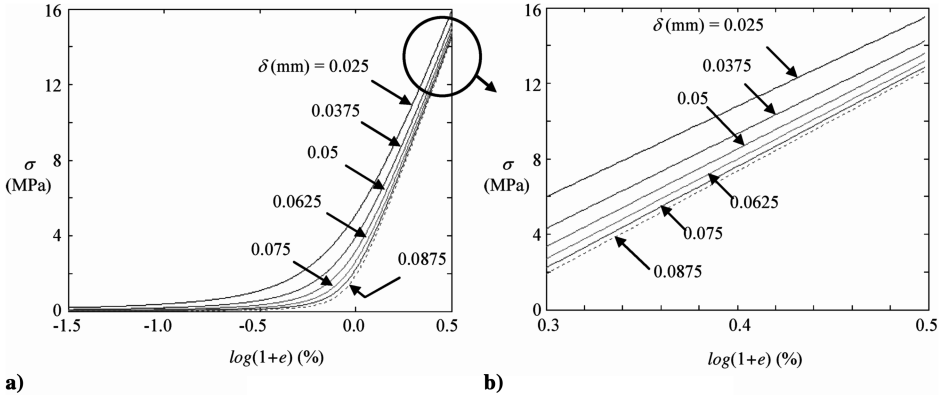

Fig. 15 Stress–strain curves with strains calculated from the original uncreased configuration for strain ranges a) between −0.015 and 0.005, and b) between 0.003 and 0.005.

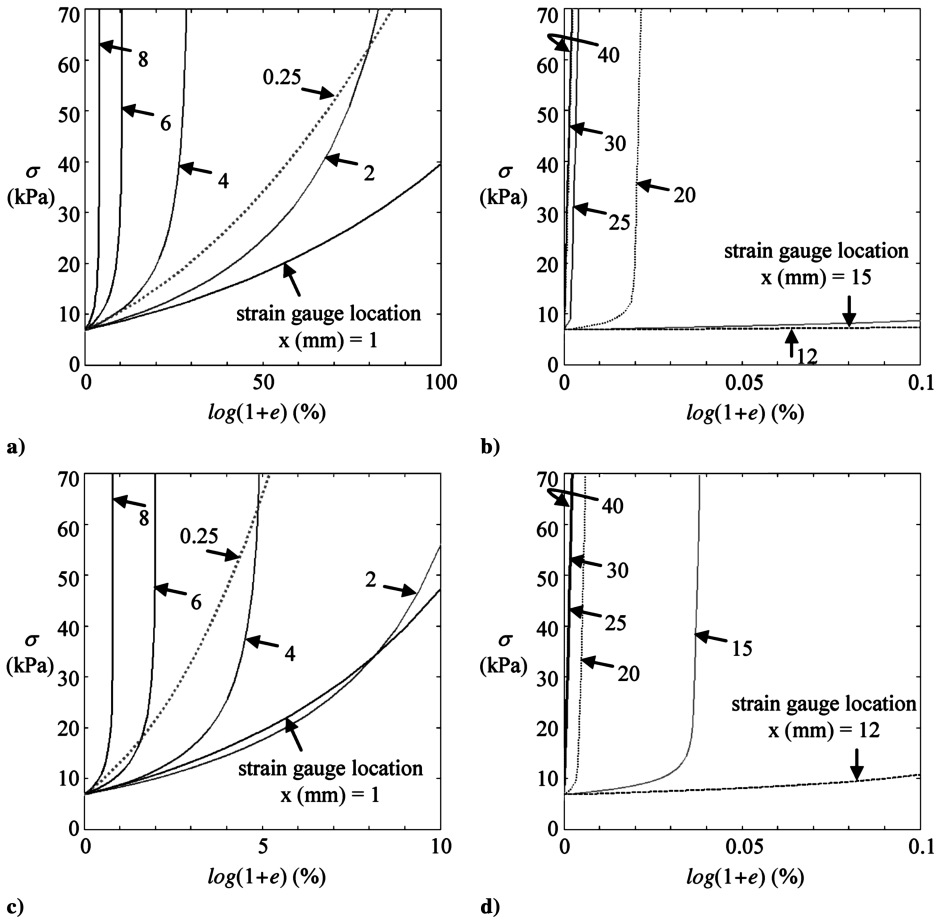

Fig. 16 Pointwise stress–strain relations under tension: a) inner gauges ($\delta = 0.025$ mm), b) outer gauges ($\delta = 0.025$ mm), c) inner gauges ($\delta = 0.0875$ mm), and d) outer gauges ($\delta = 0.0875$ mm).

crease gauges resulted in stiffer derivatives. The effective moduli calculated in this strain range approached the plane strain extensional modulus of the Kapton film as the crease gauge increased.

Figure 16 shows the variation of local stress–strain relations when the crease gauges were 0.025 and 0.0875 mm. The local strain was defined only by the x displacements and calculated using numerical strain gauges located at selected points along the center line of the membrane meshes. Figure 17 shows schematically how local strains were calculated with numerical strain gauges under tensile loads of 6.9 and 69 kPa. The arrows indicate the gauge points and the gauge length was 0.5 mm in the uncreased configuration. The local strain at the gauge point shown in the figure under 69 kPa load, for example, is defined as

$$e = \frac{\Delta l^{69\ \mathrm{kPa}} - \Delta l^{6.9\ \mathrm{kPa}}}{\Delta l^{6.9\ \mathrm{kPa}}} \tag{3}$$

The local stress–strain relations were plotted to determine whether the membrane behavior was extensional or flexural at various points under the applied tension load level. As can be seen in Figs. 16b and 16d, the stress–strain relationships became immediately linear for outer gauge points at $x = 40$ mm and 30 mm, from which one can see that these points behaved extensionally even under a very small load level. For midgauge points, the stress–strain relationships were initially nonlinear when the stress was small, which delayed the linear relationships. However, it became linear as the tensile load

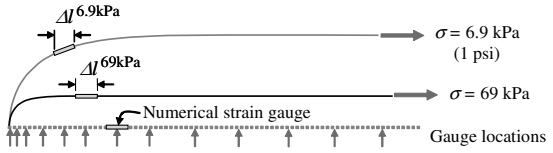

Fig. 17 Schematic deformed shapes with numerical strain gauges under tensile loads of 6.9 and 69 kPa. The arrows indicate the gauge points in the uncreased configuration.

increased. The linearity was slightly weaker for the case when $\delta = 0.025$ mm, which has a larger creased region than the case when $\delta = 0.0875$ mm. At inner gauge points near the creased region, the stress–strain relationships were fully nonlinear and produced very large strain values. Until stretched out by high tensile loads, the membrane near the creased region exhibited a significant curvature, which tried to straighten when the tensile load was applied. This bending deformation produced the large nominal strain values and was the primary source of the nonlinearity.

Note that the stress–strain relation of the inner strain gauges at $x = 0.25$ mm when $\delta = 0.025$ mm and at $x = 0.25$ mm and $x = 1$ mm when $\delta = 0.0875$ mm behaved differently. This is due to the proximity to the symmetric fold line. As discussed previously, the membrane underwent a large amount of bending deformation. Located very near to the symmetry line, however, the inner gauge at $x = 0.25$ mm had less rotation than the gauge at $x = 1$ mm, resulting in less nominal strain value. Consequently, the stress was higher for the same strain for the gauge at $x = 0.25$ mm than the ones at $x = 1$ mm or 2 mm. When the tensile load continued to increase, however, the outer curved portion of the membrane was stretched out faster than the inner part, and had smaller increase in strains. For the case when $\delta = 0.025$ mm, the initially smaller stress for the gauge at $x = 1$ mm eventually became higher than the one at $x = 0.25$ mm, though not shown in the strain range of Fig. 16a. A similar trend was observed in Fig. 16c for $\delta = 0.0875$ mm.

Figure 18 shows the effective moduli when the crease gauges were 0.025 and 0.0875 mm. The effective moduli ($E^*_{45\ \mathrm{mm}}$) were calculated by curve fitting first the stress–strain relations shown in Fig. 14, and then taking derivatives of those. The figure shows that the effective moduli of creased membrane were highly nonlinear. As discussed previously, the flexural behavior of the creased portion of the membrane under tensile loads was the primary source of the nonlinearity. As with the stresses, the effective moduli were initially very small and increased slowly for large strain ranges before showing sudden increase.

In this study, the length of the uncreased Kapton membrane model was fixed to be 45 mm. Because the nominally tensile behavior of creased membranes consisted of both tensile and flexural behavior, the nonlinear effective moduli would be dependent on the specimen size. If one needs to obtain the effective moduli for creased membranes with different sizes for use in further study such as wrinkle analysis, one can get those by repeating the creasing-tensile test simulations for the changed sizes. An easier way is to use a simple series spring model. Assume that the nonlinear effective modulus $E^*(\sigma)$ for the creased membrane with the length $L^*(\sigma)$ is available (see Fig. 1). The effective modulus for the same creased membrane with a larger length $L^{*\prime}(\sigma)$ can be calculated using the creased modulus and the pristine modulus (E) as

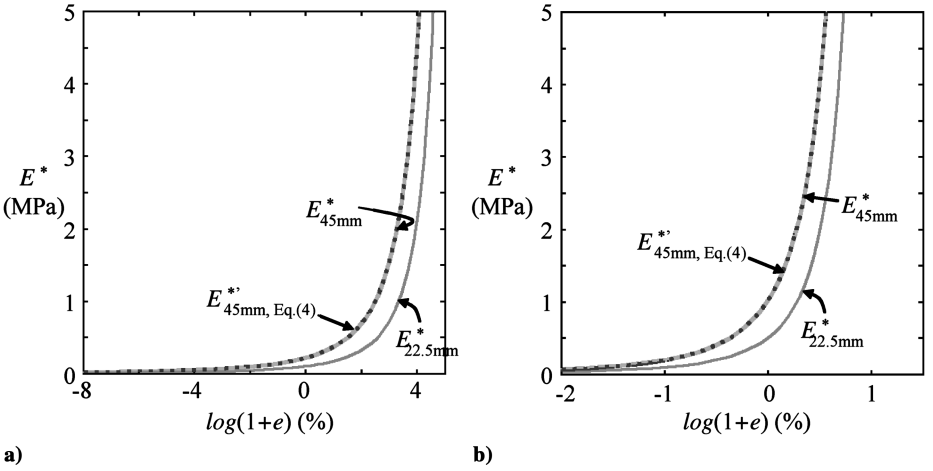

Fig. 18 Variation of effective moduli of creased Kapton membrane: a) $\delta = 0.025$ mm, and b) $\delta = 0.0875$ mm.

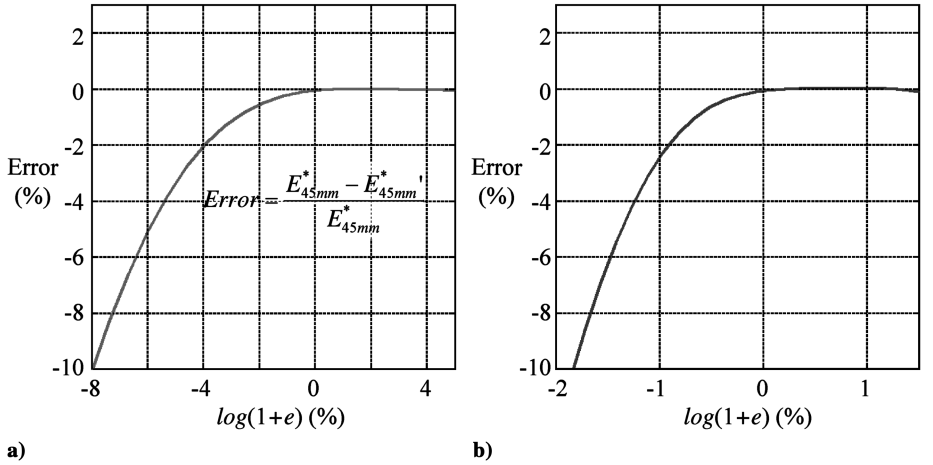

Fig. 19 Percent difference of the effective moduli calculated by Eq. (4): a) $\delta = 0.025$ mm, and b) $\delta = 0.0875$ mm.

$$\frac{1}{E^{*\prime}(\sigma)} = \frac{L^*(\sigma)}{E^*(\sigma)} + \frac{\tilde{L}(\sigma)}{E} \tag{4}$$

Here, $\tilde{L}(\sigma) = L^{*\prime}(\sigma) - L^*(\sigma)$ indicates the length of the straight elastic portion which is calculated as

$$\tilde{L}(\sigma) = \tilde{L}_0\left(1 + \frac{\sigma}{E}\right) \tag{5}$$

where $\tilde{L}_0$ is the original length of the elastic portion of the membrane, and σ the current applied tensile load.

The moduli by Eq. (4) were calculated using a half-length model (i.e., $L_0 = 22.5$ mm at zero-load uncreased state), and plotted in Fig. 18 by dotted lines. Also shown in the figure is the effective modulus of 22.5 mm membrane ($E^*_{22.5\text{ mm}}$) which was calculated first to be used in Eq. (4). When compared to the finite element analysis results for the full 45-mm length model, this modulus by the spring model with the half-length analysis result agreed fairly well. Figure 19 shows the relative percent errors in the moduli by the spring model. As can be seen in the figure, the errors were less than 1% for positive strain ranges that correspond to load level greater than 6.9 kPa (=1 psi). For the load level less than 6.9 kPa, the error increased significantly. This was due to the fact that the loaded tip of the 22.5-mm model did not yet fully reach its horizontal asymptote under the load level less than 6.9 kPa, and even the 45-mm model under the load level less than 1.5 kPa, which practically nullified the validity of the calculated moduli. To obtain the moduli in very small load ranges, longer models are needed in the creasing-tensile simulations that would reach the asymptotes under the considered tensile load.

V. Conclusions

In this paper, tensile behavior of creased membranes was studied by numerical simulations. Geometrically and materially nonlinear contact analyses were performed to simulate the process of membrane creasing. Then numerical tensile tests were performed to calculate the effective moduli. The creased and tensile geometries were also obtained by experiments and theoretical computations, respectively, and the results were compared. The creased geometry and the effective moduli were systematically investigated focusing on the variation of the crease angle and the effective moduli for various crease gauges. A simple spring model was employed to calculate the effective moduli of creased membranes with different sizes. Previous analysis [7] was limited to tightly creased cases in which the initial crease angle was assumed to be 90 deg. However, the current results suggest that the tensile behavior of creased thin membranes was dependent significantly on how hard the membranes were creased. The specific contribution of this work to the field is the use of numerical experiments to determine the initial crease angles and then calculate the effective crease modulus of thin polymer films. Simulation is required due to the extreme measurement challenges involved with physical experiments that make the determination of this key material property cost prohibitive.

Acknowledgments

The authors wish to thank the NASA In-Space Propulsion Office for partial support of this work.

References

[1] Jenkins, C. H. (ed.), *Gossamer Spacecraft: Membrane and Inflatable Structures Technology for Space Applications*, AIAA, Reston, VA, 2001.

[2] Miura, K., "Method of Packaging and Deployment of Large Membranes in Space," *Proceedngs of the 31st IAF Congress*, IAF, Tokyo, Japan, Sept. 1980.

[3] Horner, G. C., and Elliot, M. D., "A Fabrication and Deployment Approach for a Miura-Ori Solar Sail Model," AIAA Paper 2002-1708, 22–25 April 2002.

[4] Papa, A., and Pellegrino, S., "Mechanics of Systematically Creased Thin-Film Membrane Structures," AIAA Paper 2005-1975, 18–21 April 2005.

[5] Murphey, T. W., "A Nonlinear Elastic Constitutive Model for Wrinkled Thin Films," Ph.D. Dissertation, University of Colorado, Boulder, CO, 2000.

[6] Gough, A., Hossain, A., Jenkins, C. H., Blandino, J., and Hendricks, A., "Experimental and Numerical Study of Creased Membranes," AIAA Paper 2005-1976, 18–21 April 2005.

[7] MacNeal, R., and Robbins, W., "Tensile Properties of a Tape with a Transverse Crease," Astro Research Corporation, Rept. ARC-R-241, 1966.

[8] Murphy, D., Trautt, T., McEachen, M., Messner, D., Laue, G., and Gierow, P., "Progress and Plans for System Demonstration of a Scalable Square Solar Sail," *Proceedings of the 14th AAS/AIAA Space Flight Mechanics Conference*, AAS, San Diego, CA, 8–12 Feb. 2004.

[9] Hossain, A., Jenkins, C. H., and Woo, K., "Nonlinear Material Response of Systematically Creased Membranes," AIAA Paper 2006-1803, 1–4 May 2006.

L. Peterson
Associate Editor